

Roles of Slab-Gliding-Induced Surface Nano-Steps in High-Voltage Instability of LiCoO₂

Wenguang Zhao,[○] Zijian Li,[○] Tongsheng Deng, Hengyu Ren, Haocong Yi, Xiaohu Wang, Feng Jin, Cong Lin, Zhihao Shen, Shiming Chen, Chunyu Xu, Zijin Xu, Zhefeng Chen, Dong Zhou, Jun Wang, Bin Fei,* Shunning Li,* Feng Pan,* and Qinghe Zhao*



Cite This: <https://doi.org/10.1021/jacs.5c20351>



Read Online

ACCESS |



Metrics & More

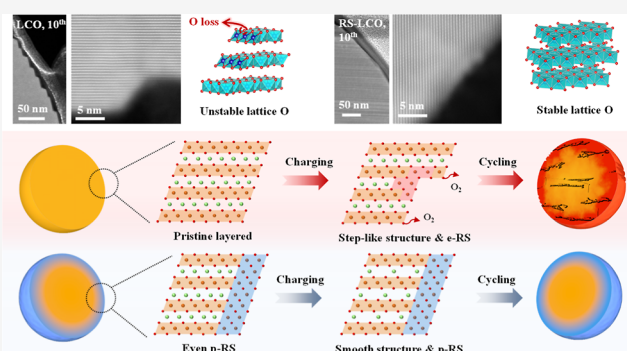


Article Recommendations



Supporting Information

ABSTRACT: Rapid capacity decay caused by lattice oxygen (lattice-O) loss under high-voltage operation remains a critical challenge for layered LiCoO₂ (LCO) cathodes. Recently, various surface modification strategies have been explored to suppress lattice-O loss, yet the underlying mechanisms remain controversial. Herein, we identify slab-gliding-induced surface nanosteps on LCO and elucidate their role in driving lattice-O loss. These nanosteps (10–20 nm per step) are induced by local Co–O slab gliding during phase transitions upon deep delithiation, thereby exposing numerous active lattice Oⁿ⁻ (0 < n < 2) sites on the (003) and (104) planes, where oxygen vacancies (O_{Vs}) can form with significantly reduced formation energies. Consequently, this accelerates lattice-O loss and promotes the formation of a surface Li⁺-blocking layer, ultimately causing a rapid capacity decay. We further demonstrate that even if a rock-salt (RS) phase forms electrochemically in situ (e-RS) on the LCO surface, it fails to suppress the lattice-O loss due to the emergence of surface nanosteps. In contrast, a prefabricated RS layer (p-RS) with enhanced mechanical robustness effectively inhibits the formation of such nanosteps, thereby intrinsically suppressing lattice-O loss during cycling. This work identifies slab-gliding-induced surface nanosteps as a key structural trigger for lattice-O loss and demonstrates that prefabricated RS coatings offer an effective route to stabilize high-voltage LCO cathodes.



1. INTRODUCTION

LiCoO₂ (LCO), one of the most widely used layered oxide cathodes, has dominated the portable consumer electronics market since its commercialization in 1991 due to its high theoretical capacity (274 mAh g⁻¹), high tap density, and excellent electronic/ionic conductivity.^{1–3} To meet the increasing energy-density demands for next-generation devices, its charge cutoff voltage has been pushed from 4.2 V to beyond 4.55 V (*vs* Li⁺/Li).^{4,5} However, this high-voltage operation triggers a cascade of coupled surface–bulk degradation issues. Specifically, upon deep delithiation with H1–3 and O1 phase transitions, the Co–O bond covalency strengthens, leading to lattice oxygen (lattice-O) oxidation/migration and subsequent loss.^{6–8} The resulting oxygen vacancies (O_{Vs}) further drive Co migration, followed by the conversion of the surface layered phase into spinel or rock-salt (RS) phases, aggravating parasitic interfacial reactions and leading to the formation of a porous cathode–electrolyte interphase (CEI).^{9,10} This porous CEI causes a rapid increase in interfacial impedance, accelerated capacity fade, and elevated safety risks.^{11–15} Therefore, simultaneously suppressing surface lattice-O loss and structural

collapse during high-voltage cycling is essential for extending the service life of LCO cathodes.^{16,17}

At higher charging voltages (>4.5 V) under deep delithiation, LCO undergoes a series of structural transitions from the O3 layered structure to a mixed O3/O1 stacking (H1–3) and eventually to the O1 (CoO₂) phase. These phase transitions are accompanied by gliding of adjacent Co–O slabs along the (003) basal plane and induce a pronounced contraction of the *c*-axis (interlayer spacing), generating substantial internal stress within the particles and thereby degrading structural stability. In fact, Dahn and co-workers initially demonstrated that the detrimental H1–3→O1 transition around 4.63 V is driven by shear gliding of the Co–O slabs and is essentially irreversible.¹⁸ This shear-induced slab gliding propagates along specific crystallographic

Received: November 15, 2025

Revised: March 27, 2026

Accepted: March 31, 2026

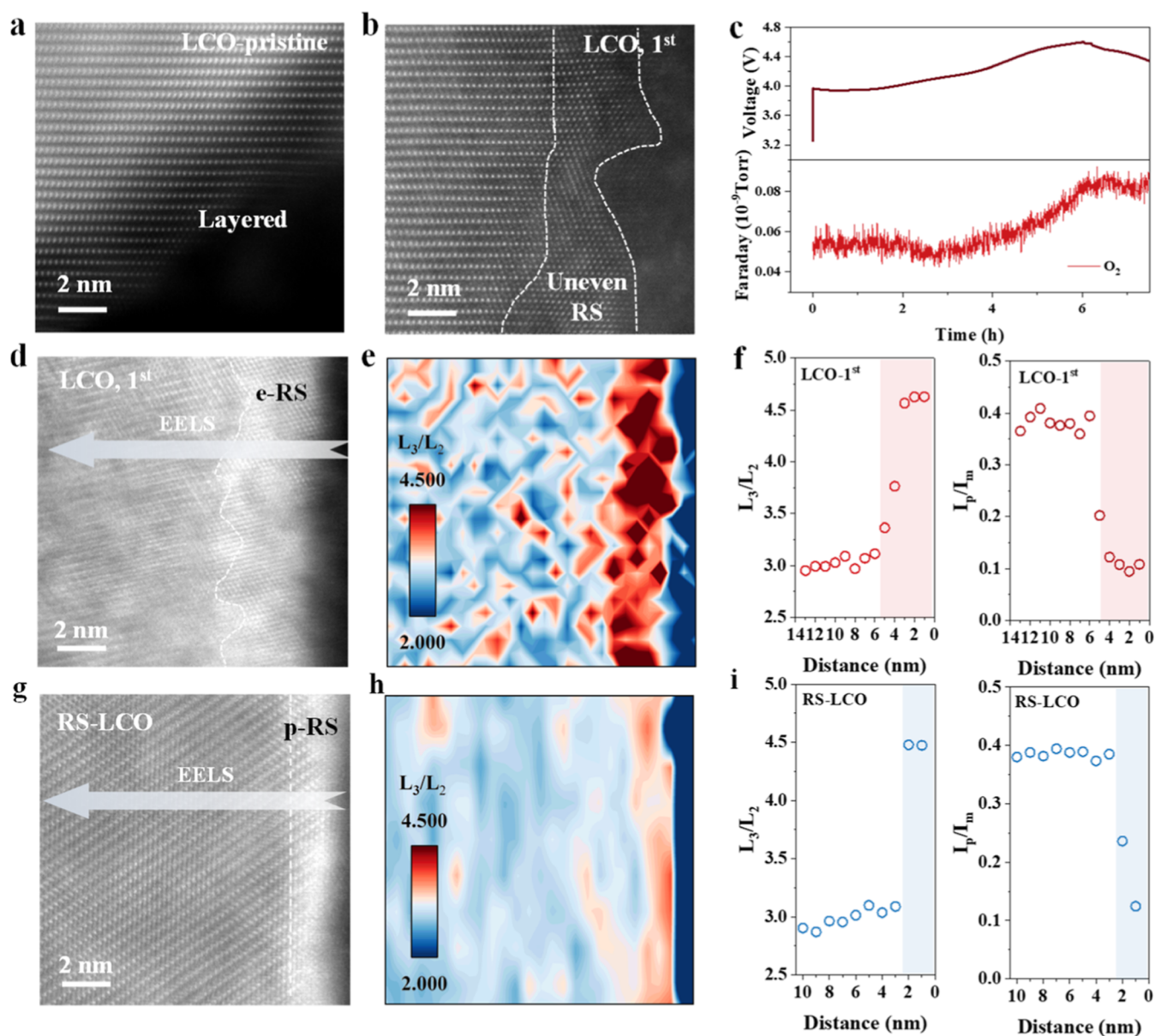


Figure 1. Surface structures of LCO and RS-LCO. HAADF-STEM images of (a) pristine LCO and (b) LCO after the first cycle. (c) DEMS curve during the first cycle. High-resolution HAADF-STEM images of (d) LCO after the first cycle and (g) RS-LCO, (e,h) corresponding EELS mapping, and (f,i) corresponding L_3/L_2 (Co L-edge) and I_p/I_m ratios (O K-edge) extracted from EELS data, with the scan directions and distances indicated in (d) and (g), respectively.

directions to generate nanoscale surface terraces, whose highly reactive step sites further accelerate surface lattice-O loss.¹⁹ Consequently, a crucial mitigation strategy is mechanical stabilization of the surface to suppress slab gliding. For instance, an ultrathin Al_2O_3 coating has been shown to inhibit the H1–3/O1 shear transition and preserve structural reversibility under high-voltage operation.²⁰ Our previous work further revealed that a rock-salt surface structure can mechanically anchor the Co–O slabs, stabilize lattice-O, and effectively suppress oxygen release.²¹

Previous studies have developed various surface-structure reinforcement strategies, such as preconstructing nonlayered fluoride and phosphate coatings on the LCO surface to isolate the electrolyte from active surface lattice O^{n-} ($0 < n < 2$) species and thereby mitigate parasitic side reactions.¹⁸ Among these, rock-salt (RS) phases are particularly attractive owing to

their stabilized lattice frameworks, excellent lattice match with the layered phase, and relatively low Li^+ diffusion barriers.^{22,23} An important but often overlooked point is that a surface RS phase can either form in situ during electrochemical cycling (thus termed e-RS) or be prefabricated ex situ (p-RS) before cycling. Although high-resolution micrographs of the two variants appear nearly identical, experiments consistently show that e-RS fails to halt surface degradation, whereas p-RS markedly enhances surface stability.^{5,24,25} However, the underlying mechanism for these observations remains unclear. Therefore, a comprehensive comparison of the characteristics of the e-RS and p-RS phases, including their spatial distributions, chemical states, and Li^+ transport kinetics, is essential for elucidating the crucial role of p-RS in enhancing the surface lattice-O stability and high-voltage cycling performance of LCO cathodes.

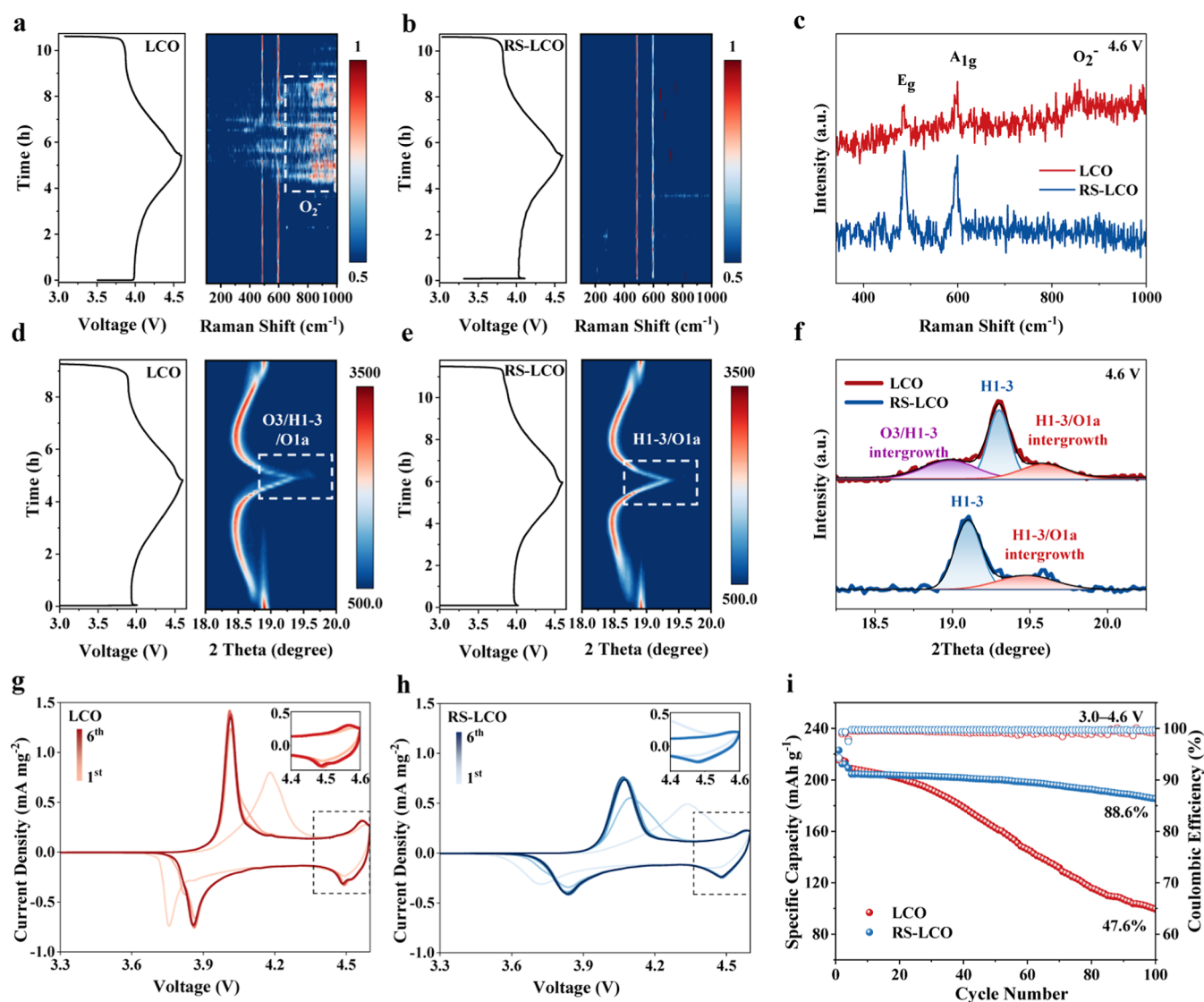


Figure 2. Structural evolution and electrochemical performance of LCO and RS-LCO. In situ Raman spectroscopy of (a) LCO and (b) RS-LCO during the first cycle. (c) Raman spectra of LCO and RS-LCO at 4.6 V. In situ XRD patterns of (d) LCO and (e) RS-LCO during the first cycle and (f) selected XRD patterns of LCO and RS-LCO at 4.6 V. Cyclic voltammetry curves of (g) LCO and (h) RS-LCO during the initial six cycles. (i) Long-term cycling performance of LCO and RS-LCO at 1 C.

Herein, by combining advanced electron microscopy, in situ spectroscopy, electrochemical analyses, and density functional theory (DFT) calculations, we systematically distinguish surface e-RS and p-RS phases on commercial LCO cathodes and elucidate their specific influences on cycling stability. We reveal that, during initial charging to 4.6 V, discontinuous and nonuniform e-RS domains emerge on the bare LCO surface, accompanied by the formation of slab-gliding-induced nanosteps (10–20 nm per step) at a high state of charge (SOC). These nanosteps exhibit significantly lower O_V formation energies compared to terrace sites, owing to the under-coordinated lattice oxygen, local strain, and charge redistribution at the step edges. These low-energy step sites are inherently more reactive, facilitating lattice-O loss. With repeated nanostep formation and disappearance during high-voltage cycling, the in situ-formed e-RS layer continuously thickens and eventually evolves into a Li^+ -blocking layer. In contrast, a continuous, uniform, and mechanically robust p-RS coating constructed prior to cycling effectively suppresses nanostep formation and surface lattice-O loss. Moreover, p-RS

efficiently suppresses interfacial side reactions and promotes the formation of an inorganic-rich, robust cathode-electrolyte interphase that preserves surface structural integrity. This work underscores that the formation of slab-gliding-induced nanosteps is a primary driving force behind accelerated lattice-O loss and fundamentally explains why the prefabricated p-RS phase outperforms the in situ e-RS phase in stabilizing LCO cathodes. Furthermore, we propose a stabilization pathway by which surface lattice-O loss can be effectively mitigated.

2. RESULTS AND DISCUSSION

2.1. Structural Comparison of Surface e-RS and p-RS Phases

Commercial LCO with a typical α - $NaFeO_2$ structure was used in this study (Figure S1 and Table S1). Its pristine surface exhibits a pure layered phase (Figure 1a), providing a clear baseline for tracking the surface evolution from the layered phase to the e-RS phase. After the initial cycle in the voltage range of 3.0–4.6 V at 0.2C ($1C = 200 \text{ mA g}^{-1}$), a surface phase

transition occurs, and a nonuniform e-RS phase layer with a thickness of 1–4 nm forms on the LCO surface, as shown by atomic-resolution high-angle annular dark-field scanning transmission electron microscopy (HAADF-STEM, Figure 1b). To elucidate the e-RS phase evolution, differential electrochemical mass spectrometry (DEMS) was performed during the first cycle (Figure 1c). A gaseous O₂ signal was detected once the voltage exceeded 4.4 V, confirming lattice-O loss from the LCO. The formation of the surface e-RS phase was further corroborated by HAADF-STEM and electron energy-loss spectroscopy (EELS).²⁶ Specifically, after the first cycle, an e-RS phase was already discernible on the LCO surface (Figure S2), and both EELS mapping and line scans (Figure 1d–f) revealed a markedly lower Co valence (i.e., higher L₃/L₂ and lower I_p/I_m ratios),²⁷ thus confirming surface lattice-O loss.^{28,29}

Prefabricating an RS phase is an effective surface reinforcement strategy for layered cathodes. By treating LCO with H₃BO₃, a uniform p-RS layer was constructed on the LCO surface (RS-LCO). Although this p-RS appears structurally similar to the e-RS in the HAADF-STEM images, the two cathodes exhibit markedly divergent electrochemical behaviors. We therefore focus on clarifying these distinctions. Fundamentally, the different formation mechanisms account for the distinct spatial distributions of the RS phase: p-RS originates from a homogeneous chemical reaction process in solution, yielding uniform thickness and defect distribution, whereas e-RS forms via localized slab-gliding and nanostep-triggered electrochemical reconstruction under high-voltage deep delithiation, which is driven by local stress and oxygen loss and thus leads to an inherently heterogeneous surface structure. As shown by the X-ray diffraction (XRD) Rietveld refinement results in Figure S3 and Table S2, the bulk phase of RS-LCO is almost identical to that of bare LCO, while a uniform p-RS layer with a thickness of ~2 nm is observed on the surface (Figures 1g and S4), in sharp contrast to the nonuniform e-RS layer. EELS mapping and line profiles (Figures 1h,i and S5) further highlight the pronounced differences between the surface p-RS phase and the bulk layered phase. Specifically, the distribution of low-valence Co on the RS-LCO surface shows a continuous and uniform character of the p-RS phase, in contrast to that of e-RS on the LCO surface.

2.2. Lattice-O Stability and Phase Transition Reversibility

We directly probed the lattice-O stability of LCO and RS-LCO under high-voltage cycling using in situ Raman spectroscopy (Figure 2a–c). For bare LCO, the E_g (~485 cm⁻¹) and A_{1g} (~595 cm⁻¹) modes progressively decrease when the voltage exceeds 4.5 V, while a new band emerges at ~860 cm⁻¹, attributed to the O–O stretch of peroxide-like (O₂)ⁿ⁻ species,^{30,31} demonstrating that lattice-O is extracted and dimerized at the LCO surface. In sharp contrast, both the E_g and A_{1g} modes of RS-LCO are retained even when charged to 4.6 V, and no peroxide feature is detected, demonstrating that the surface p-RS phase efficiently stabilizes lattice-O against oxidation and dimerization.

Lattice-O stability also significantly affects the interfacial and surface impedance. Figures S6 and S7 show the in situ electrochemical impedance spectroscopy (EIS) and correlated distribution of relaxation times (DRT) results of LCO and RS-LCO during the initial two and long-term cycles. The DRT peaks in the relaxation-time (τ) ranges of 10⁻⁴–10⁻² and

10⁻²–10⁻¹ s correspond to Li⁺ transport across the CEI (i.e., R_{CEI}) and across the near-surface structure (i.e., R_{ct}), respectively. Notably, the LCO cell exhibits substantial variations in both R_{ct} and τ , indicating significant surface reconstruction to form an e-RS phase, while the p-RS phase on the RS-LCO surface remains stable, as reflected by the minor R_{ct} and τ changes.³² After long-term cycling, the impedance of LCO becomes significantly higher than that of RS-LCO due to severe surface structural reconstruction caused by nanosteps, indicating severe hindrance to electron and Li⁺ diffusion.

Figure 2d–f shows the in situ XRD patterns of LCO and RS-LCO during the first cycle. The XRD patterns obtained at 4.6 V, extracted from in situ measurements, are illustrated in Figure 2f. Compared with LCO, the H1–3 peak of RS-LCO appears at a lower 2 θ angle, indicating that the p-RS structure suppresses the high-voltage phase transition. It is worth noting that the phase transition in LCO when charged to high voltages remains nonuniform, with the O3/H1–3 phase intergrowth still present. Conversely, in RS-LCO, the homogenization of the phase transition is facilitated by p-RS-regulated Li⁺ (de)intercalation. Since this phase transition is driven by Co–O slab gliding under deep delithiation, we infer that the presence of the surface p-RS phase modulates the slab-gliding behavior, which may directly account for the structural differences observed on LCO and RS-LCO surfaces, as discussed in a later section.

The galvanostatic charge/discharge curves and cyclic voltammetry measurements for the first cycle also show the influence of the surface structure on phase transitions (Figures 2g,h and S8). Specifically, the cathodic peaks of LCO are sharper and stronger than those of RS-LCO, indicating a more concentrated redox process. In contrast, RS-LCO displays slower redox kinetics, which is attributed to the electrochemically inert lattice Co/O in the p-RS structure and thus alleviates lattice-O oxidation and dimerization in the near-surface region.

Benefiting from the suppressed lattice-O oxidation and regulated slab-gliding behavior, RS-LCO exhibits a superior cycling stability compared with LCO (Figure 2i). This is further reflected in the voltage polarization (Figure S9), which shows that the voltage variation of RS-LCO is much smaller than that of LCO, highlighting the high stability of the surface p-RS phase during cycling. Figures S10 and S11 show the galvanostatic intermittent titration technique (GITT) results and the corresponding calculated Li⁺ diffusion coefficients (D_{Li⁺}), which reflect apparent Li⁺ transport kinetics under different cycling conditions. For RS-LCO, its D_{Li⁺} values remain relatively constant, evidencing well-retained Li⁺ diffusion kinetics through the surface p-RS phase. However, the D_{Li⁺} values of LCO decrease significantly, implying deteriorated Li⁺ diffusion due to the in situ-formed e-RS phase. Such a difference in diffusion also explains the superior rate performance of RS-LCO over that of LCO (Figure S12). These results collectively indicate that the surface p-RS phase can stabilize the near-surface lattice-O, regulate Co–O slab gliding, and enhance Li⁺ diffusion kinetics, thus stabilizing the RS-LCO surface and contributing to superior electrochemical performance.

2.3. Formation of Slab-Gliding-Induced Surface Nanosteps

Electrochemical data indicate that LCO and RS-LCO have similar capacities at the 10th cycle (Figure S13); beyond the 10th cycle, their electrochemical responses diverge and LCO

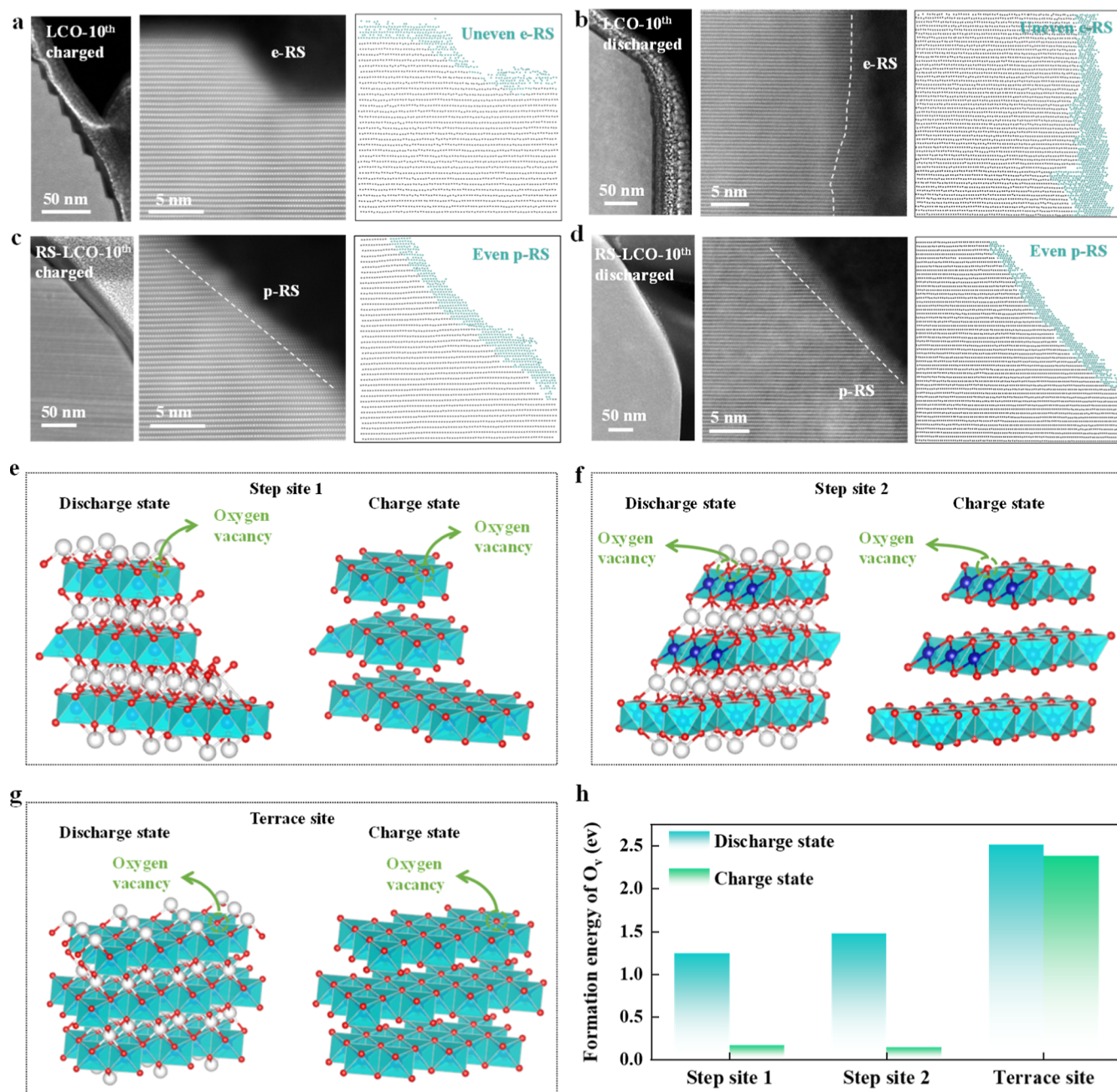


Figure 3. Surface structures and theoretical calculations. HAADF-STEM images and AI-segmented surface structures of (a) charged and (b) discharged LCO, and (c) charged and (d) discharged RS-LCO in the 10th cycle. Schematic illustrations of O_V formation at the (104) plane in (e), the (003) plane in (f), and terrace sites in (g), for both charged and discharged states. (h) Calculated O_V formation energies for the three surface sites.

shows a marked capacity decay. To further investigate the structural evolution after 10 cycles and the effects of the e-RS and p-RS coating phases on LCO, a comparative analysis of the structure and chemical states was performed for the two cathodes after the 10th cycle. Figure 3a–d shows the surface morphology and phase structure of LCO and RS-LCO at the fully charged and discharged states of the 10th cycle. For charged LCO, deep delithiation drives the O3-to-H1–3 phase transition with pronounced Co–O slab gliding, leading to the formation of surface nanosteps with a characteristic spacing of approximately 10–20 nm. Since the surface e-RS phase and surface nanosteps appear almost simultaneously, this indicates that the in situ-formed e-RS phase cannot prevent Co–O slab

gliding and nanostep formation. More detailed images of the surface nanosteps are provided in Figure S14, revealing that these nanosteps consist of both newly exposed and original surfaces. For each nanostep, the newly exposed surfaces are parallel to the Co–O slabs and are hereafter referred to as “terrace sites”, whereas the intersections between the newly exposed and original surfaces are termed the “step sites”. Artificial intelligence (AI)-segmented analysis of the surface structure further distinguishes layered and RS regions, revealing a layered/RS hybrid structure on the charged LCO surface.^{33–35} Upon discharge, the LCO surface recovers from a stepped morphology back to a smooth morphology with a pure

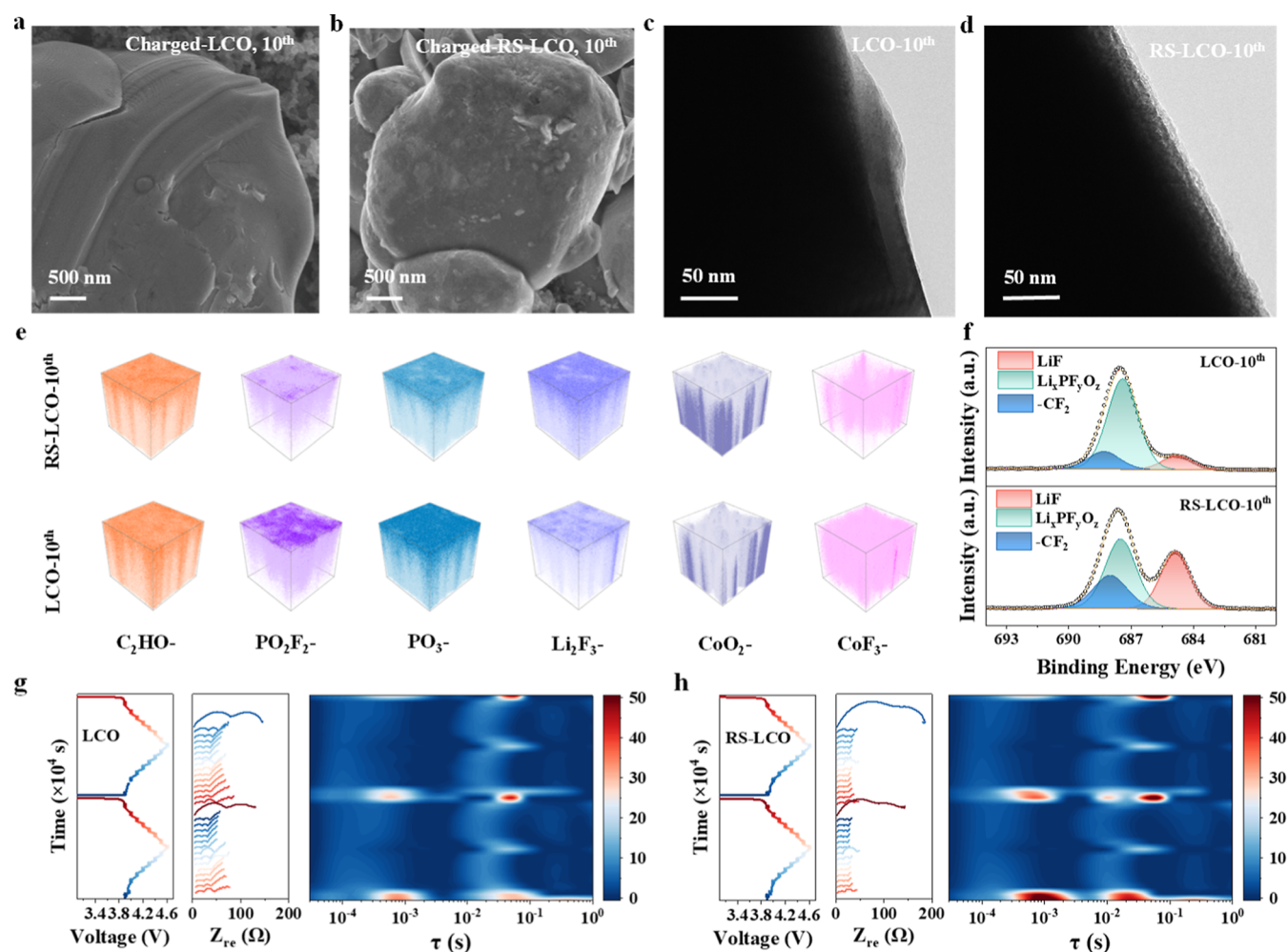


Figure 4. Surface morphology, composition, and interfacial reactions of LCO and RS-LCO. SEM images of charged (a) LCO and (b) RS-LCO at the 10th cycle. TEM images of charged (c) LCO and (d) RS-LCO at the 10th cycle. (e) TOF-SIMS depth profiles and (f) F 1s XPS spectra of the discharged LCO and RS-LCO after the 10th cycle. In situ EIS and DRT analyses of (g) LCO and (h) RS-LCO in the 10th and 11th cycles.

e-RS phase, indicating the repeated emergence and disappearance of terrace sites.

For LCO, the surface e-RS phase forms after just one cycle. However, it is unable to inhibit Co–O slab gliding in subsequent cycles, thereby significantly accelerating surface exposure and lattice-O loss. Figures S15 and S16 show the EELS results of LCO after the 10th charge. Specifically, the Co L-edge L_3/L_2 ratios (in the 2.5–4.5 range) and the O K-edge I_p/I_m ratios (in the 0.1–0.5 range) are distributed over a wide range, indicating an uneven valence distribution. In comparison, the p-RS phase remains intact on the RS-LCO surface after both the 10th charge and discharge (Figure 3c,d), highlighting its exceptional structural stability and mechanical toughness. More importantly, the charged RS-LCO surface exhibits a smooth morphology without obvious nanosteps, indicating that Co–O slab gliding is effectively suppressed, consistent with the delayed O3–H1–3 phase transition observed by in situ XRD (Figure 2f). Furthermore, EELS shows that the Co valence at the charged RS-LCO surface is more concentrated (with L_3/L_2 ratios in the 4.0–4.5 range and I_p/I_m ratios in the 0.1–0.2 range) than that of LCO (Figures S17 and S18), which correlates with the high structural stability of the surface p-RS phase.

Based on the above analysis, the e-RS phase forms concomitantly with surface nanosteps, a rarely reported type

of defective structure that further facilitates the pronounced O_V formation in the near-surface region of LCO. To gain deeper insight, density functional theory (DFT) calculations were carried out using a surface model that exposes two representative step planes, i.e., (104) and (003), and a defect-free terrace, and the O_V formation energies were evaluated in both charged and discharged states. The results shown in Figure 3e–h suggest that the O_V formation energy at terrace sites is significantly higher than that at step sites (site 1 and site 2 for (104) and (003) planes, respectively) for both charged and discharged states, demonstrating that surface nanosteps promote lattice O_V formation. Moreover, for all scenarios, the O_V formation energies in the charged state are consistently lower than those in the discharged state, implying that lattice O_V formation is more pronounced in the charged states, which is also consistent with previous experimental results. Notably, during the charge process, the p-RS phase can effectively suppress the formation of slab-gliding-induced surface nanosteps, thereby avoiding active O exposure on the (104) and (003) planes. This markedly suppresses lattice-O loss and consequently reduces O_2 evolution from RS-LCO compared with LCO (Figure S19).

Based on the analysis above, the primary distinction between surface e-RS and p-RS phases lies in their mechanical ability to suppress slab-gliding-induced surface nanostep formation. The

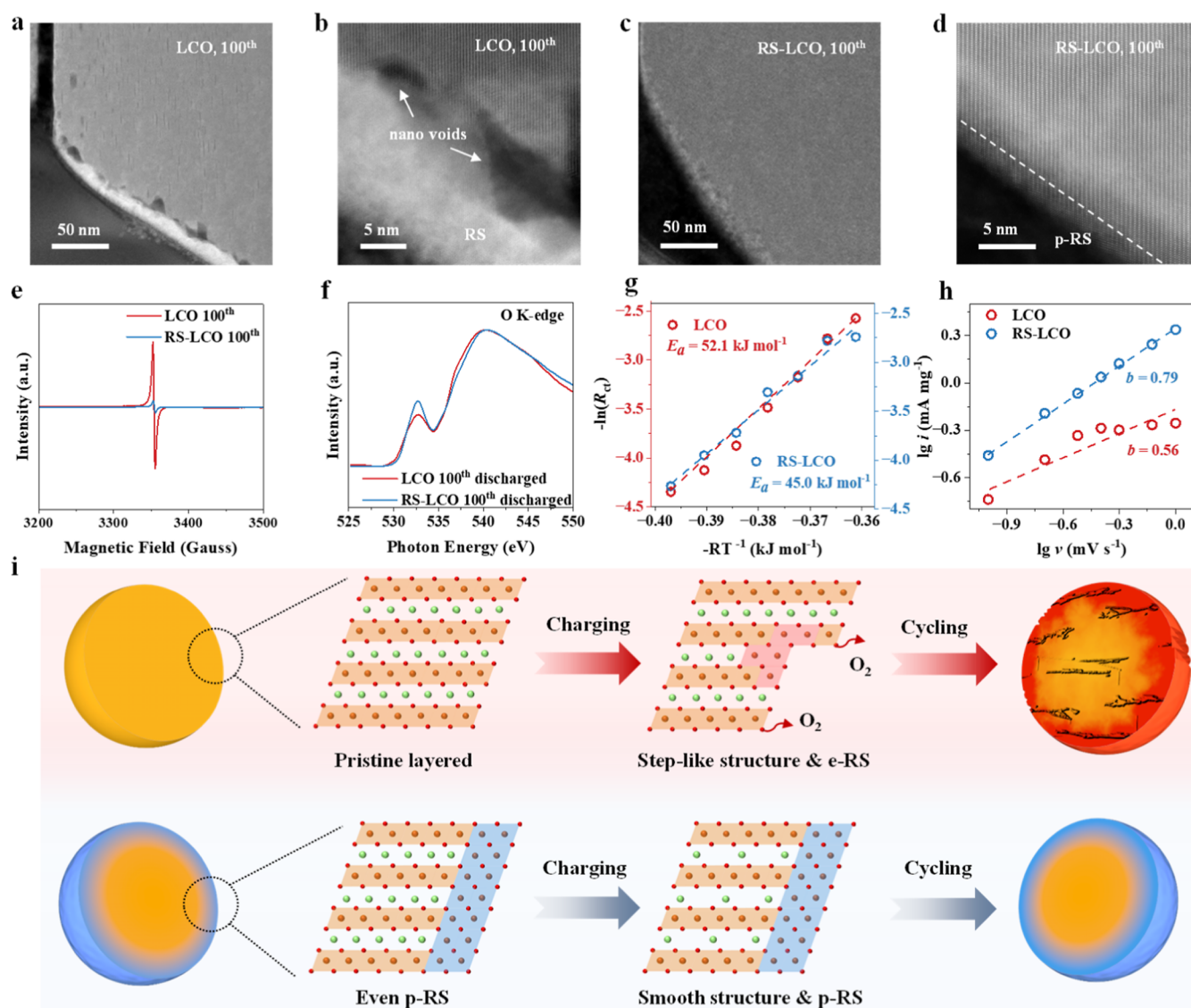


Figure 5. Surfaces of LCO and RS-LCO after long-term cycling and surface evolution. (a,c) low-magnification surface images and (b,d) high-resolution HAADF-STEM images of LCO (a,b) and RS-LCO (c,d) after the 100th cycle. (e) EPR spectra, (f) sXAS O K-edge spectra, (g) activation energies (E_a), and (h) b values of cycled LCO and RS-LCO. (i) Schematic illustration of the evolution of surface e-RS and p-RS phases upon cycling.

e-RS phase naturally emerges together with surface nanosteps, and the two features mutually reinforce each other to promote surface lattice-O loss and, in turn, thicken the e-RS phase and slow down interfacial Li⁺ transport kinetics. In contrast, the p-RS phase prevents such surface nanostep formation from the outset of cycling. This effect is attributed not only to more uniform Li⁺ (de)intercalation behavior and a higher O_V formation energy in the p-RS phase but also to the fact that the p-RS phase functions as a “rivet” in the near-surface structure, providing sufficient mechanical resistance to Co–O slab gliding and the O3-to-H1–3 phase transition. Therefore, the formation of surface nanosteps is inhibited and exposed active O sites are diminished. Consequently, RS-LCO exhibits more stable cycling performance and superior rate capability.

2.4. Interface Reactions Governed by Lattice-O Stability

Generally, the O3-to-H1–3 phase transition under high-voltage charging beyond 4.5 V inevitably generates internal stresses, especially in the surface region. As shown in Figure S20, a relatively uniform stress distribution is observed at the

charged LCO surface, indicating that these stresses can be partially relieved by forming surface nanosteps via Co–O slab gliding. In contrast, significant internal stresses persist at the charged RS-LCO surface and within the RS-LCO bulk (Figure S21), suggesting that they are effectively constrained by the surface p-RS phase. These results indicate that surface e-RS and p-RS phases differ in their ability to constrain the internal stresses induced by the O3-to-H1–3 phase transition in the near-surface region, thereby leading to distinct surface reaction pathways and, consequently, affecting the morphology and CEI composition.

Figure 4a–d compares the surface morphology of charged LCO and charged RS-LCO at the 10th cycle. For LCO, the CEI forms on the nanosteps and becomes thicker and more irregular as a result of exacerbated lattice-O release, further evolving into an even more heterogeneous layer after 100 cycles (Figure S22). In stark contrast, RS-LCO exhibits a significantly more uniform and thinner CEI, indicating more favorable interfacial reactions. Furthermore, time-of-flight

secondary ion mass spectrometry (TOF-SIMS) results show that the CEI layer on the LCO surface after 10 cycles contains higher amounts of C_2HO^- , P-containing, and Co-containing species, originating from organic solvent and PF_6^- decomposition as well as Co dissolution, whereas the CEI on RS-LCO is enriched in F-containing species (Figure 4e). Because F-containing species are critical for forming a robust CEI, their enrichment highlights the denser and more robust nature of the CEI on RS-LCO. Meanwhile, more abundant active O sites on the e-RS phase foster the formation of a larger quantity of decomposition products in the CEI layer, as revealed by X-ray photoelectron spectroscopy (XPS) (Figures 4f and S23). Specifically, in the O 1s spectra, LCO after the 10th cycle exhibits a pronounced lattice-O component, likely arising from the newly exposed terrace sites in the nanosteps. Importantly, the CEI on RS-LCO features a slightly increased P–O peak intensity and higher levels of $Li_xPF_yO_z$ species, indicative of a larger inorganic fraction in the CEI. Similarly, the F 1s spectra show consistently higher LiF content in the CEI of RS-LCO, which enhances the robustness, density, and chemical stability of the CEI and thereby benefits the cycling performance of RS-LCO.

Additionally, interfacial reaction behavior was evaluated by in situ EIS and the corresponding DRT analyses for LCO and RS-LCO in the 10th and 11th cycles (Figure 4g,h). Specifically, LCO shows more pronounced changes in impedance, especially for R_{ct} , indicating that the e-RS phase undergoes a significant structural evolution during repeated local Co–O slab gliding. In contrast, due to the higher structural and lattice-O stability of the p-RS phase, RS-LCO exhibits much smaller changes in both R_{ct} and R_{CEI} , consistent with significantly mitigated interfacial reactions.

2.5. Stabilized Lattice-O in RS-LCO During Long-Term Cycling

Surface e-RS and p-RS phases have different capabilities to stabilize lattice-O, leading to distinct surface structures during long-term cycling. For the LCO cathode, the surface becomes densely populated with pronounced nanosteps at the 100th cycle, while the RS-LCO surface remains relatively smooth (Figure 5a,c). In more detail, cycled LCO exhibits a thickened surface e-RS phase, whereas the RS-LCO surface after cycling retains a thin p-RS layer with a thickness comparable to that of pristine RS-LCO (Figures 5b,d). Further regarding the thickness evolution of surface RS phase during long-term cycling, it is obvious from Figure S24 that e-RS exhibits a rapid thickening trend, whereas the thickening rate of p-RS is significantly slower. This comparison directly demonstrates the effectiveness of the p-RS strategy in suppressing the continuous thickening of the RS layer. Although the electron paramagnetic resonance (EPR) spectra of LCO and RS-LCO collected at the 10th cycle seem similar (Figure S25), the EPR signal becomes much more pronounced for LCO at the 100th cycle, indicating a significantly increased O_V content (Figure 5e). Furthermore, soft X-ray absorption spectroscopy (sXAS) acquired in total-electron-yield (TEY) mode shows that the O K-edge I_p/I_m ratio of LCO drops sharply after long-term cycling (Figure 5f), confirming the accumulation of O_V s in the near-surface region.^{21,36} These results corroborate DFT calculations, demonstrating that the surface nanosteps on LCO facilitate continuous lattice-O loss during long-term cycling, leading to O_V accumulation in the near-surface region. In contrast, in RS-LCO, the p-RS phase suppresses both nanostep formation and

lattice-O release, resulting in a lower surface O_V concentration. Consequently, RS-LCO retains a well-ordered layered structure even after 100 cycles, as evidenced by a higher $I_{(003)}/I_{(104)}$ ratio in the XRD pattern (Figure S26), thereby underscoring the superior structural stability conferred by the surface p-RS phase.

To isolate and quantify the surface Li^+ transport kinetics of cycled LCO and RS-LCO, variable-temperature EIS tests were further employed. Using the charge-transfer resistance (R_{ct}) measured in the near-surface region after 100 cycles, we extracted the activation energy (E_a) for Li^+ migration. The calculated E_a values indicate that Li^+ encounters a significantly lower transport barrier in p-RS than in e-RS (Figure 5g and S27). Multiscan-rate cyclic voltammetry was then employed to determine b values, yielding $b = 0.54$ for LCO and $b = 0.79$ for RS-LCO (Figures 5h and S28). The higher b value of RS-LCO indicates that its surface retains abundant charge-storage sites, which generally correlate with superior rate capability. In contrast, after long-term cycling, the LCO surface is covered by a thick e-RS phase and experiences extensive lattice-O participation in charge compensation, thus lowering surface reactivity, weakening the pseudocapacitive response, and driving the b value toward the diffusion-controlled limit (~ 0.5). Moreover, the greater lattice-O loss further triggers additional parasitic reactions, with reaction products accumulating on the e-RS surface as a Li^+ -blocking layer, thus diminishing LCO activity and ultimately lowering the b value.

Figure S29 presents TEM images of the LCO and RS-LCO surfaces after 100 cycles. For LCO, the surface shows a loose, irregular, and thick layer, resulting from severe surface side reactions during prolonged cycling. In contrast, RS-LCO with stabilized surface lattice-O exhibits a relatively thin and uniformly distributed CEI. Further XPS analysis (Figures S30 and S31) reveals that the cycled LCO has a thickened CEI composed predominantly of organic species, which is due to the severe solvent oxidation caused by the more active e-RS surface. The relative enrichment and continuous coverage of inorganic components such as LiF are thus insufficient to form an effective dense protective layer. While a significant amount of LiF is detected in the CEI of cycled RS-LCO, indicating that the p-RS effectively suppresses lattice-O release and interface side reactions, making the CEI formation more controllable to generate a dense and uniform LiF-rich inorganic protective layer. This layer has excellent chemical stability and mechanical strength, which can effectively block the continuous penetration and decomposition of the electrolyte, thereby improving high-voltage cycling stability. Furthermore, in situ EIS and DRT analyses provide additional evidence for superior interfacial properties of RS-LCO (Figure S32), showing that both R_{ct} and R_{CEI} of RS-LCO remain stable, thereby confirming its more favorable interfacial reaction kinetics.

To better understand the mechanism, a schematic illustration is provided in Figure 5i. For LCO, during the first cycle, the e-RS phase is formed in situ on its surface, accompanied by the emergence of surface nanosteps induced by Co–O slab gliding associated with the O3-to-H1–3 phase transition under deep delithiation. These nanosteps expose numerous active lattice-O sites with lower O_V formation energies on the (003) and (104) planes, thereby facilitating lattice-O loss. During long-term cycling, a Li^+ -blocking layer consisting of a thickened e-RS phase and an uneven CEI further forms and accelerates the capacity decay. For RS-LCO, the RS phase is uniformly distributed prior to cycling and

mechanically robust, effectively suppressing surface nanostep formation, thereby significantly increasing O_V formation energies and inhibiting the generation of active O sites. As a result, the p-RS phase maintains excellent structural stability during long-term cycling and enables the superior cycling performance of RS-LCO.

3. CONCLUSIONS

This work identifies slab-gliding-induced surface nanosteps as a primary structural trigger for lattice-O loss in LCO cathodes. Upon deep delithiation with the O3-to-H1-3 phase transition, Co-O slab gliding produces surface nanosteps (with a spacing of 10–20 nm for each step) on bare LCO, which expose numerous active lattice-O sites with significantly lowered OV formation energies and thereby trigger continuous lattice-O loss. The in situ-formed e-RS layer cannot effectively block this lattice-O loss and instead thickens into a Li^+ -blocking surface layer that degrades interfacial Li^+ transport, leading to increased interfacial resistance and rapid capacity decay. In contrast, the prefabricated, uniform p-RS phase constrains Co-O slab gliding under deep delithiation and suppresses the formation of slab-gliding-induced surface nanosteps, thereby inhibiting the exposure of active lattice-O sites on RS-LCO, blocking sustained lattice-O loss, and thus enhancing structural stability during long-term cycling. Moreover, the p-RS phase also promotes the formation of a thin, uniform, and inorganic-rich CEI. These findings establish a new paradigm for the surface modification of high-voltage layered oxide cathodes: instead of in situ-formed coating phases, a prefabricated, uniform, and functional surface layer can effectively stabilize lattice-O and overcome the trade-off among energy density, rate capability, and lifetime.

■ ASSOCIATED CONTENT

SI Supporting Information

The Supporting Information is available free of charge at <https://pubs.acs.org/doi/10.1021/jacs.5c20351>.

Experimental and computational details; additional characterization results, including XRD, HAADF-STEM, EELS, DEMS, geometric phase analysis, SEM, XPS, and EPR data; additional electrochemical results, including in situ EIS, DRT, GITT, rate, variable-temperature EIS, and multiscan-rate cyclic voltammetry (PDF)

■ AUTHOR INFORMATION

Corresponding Authors

Bin Fei – School of Fashion and Textiles, The Hong Kong Polytechnic University, Hong Kong S.A.R. 999077, China; orcid.org/0000-0002-4274-1873; Email: bin.feipolyu.edu.hk

Shunning Li – School of Advanced Materials, Peking University Shenzhen Graduate School, Shenzhen 518055, China; Department of Chemical and Biological Engineering, The Hong Kong University of Science and Technology, Hong Kong S.A.R. 999077, China; orcid.org/0000-0002-5381-6025; Email: lisan@pku.edu.cn

Feng Pan – School of Advanced Materials, Peking University Shenzhen Graduate School, Shenzhen 518055, China; orcid.org/0000-0002-8216-1339; Email: panfeng@pkusz.edu.cn

Qinghe Zhao – School of Advanced Materials, Peking University Shenzhen Graduate School, Shenzhen 518055, China; College of Physics and Energy, Fujian Normal University, Fuzhou 350117, China; Email: zhaqinghe@fjnu.edu.cn

Authors

Wenguang Zhao – School of Advanced Materials, Peking University Shenzhen Graduate School, Shenzhen 518055, China

Zijian Li – School of Fashion and Textiles, The Hong Kong Polytechnic University, Hong Kong S.A.R. 999077, China

Tongsheng Deng – College of Physics and Energy, Fujian Normal University, Fuzhou 350117, China

Hengyu Ren – School of Advanced Materials, Peking University Shenzhen Graduate School, Shenzhen 518055, China

Haocong Yi – School of Advanced Materials, Peking University Shenzhen Graduate School, Shenzhen 518055, China

Xiaohu Wang – School of Advanced Materials, Peking University Shenzhen Graduate School, Shenzhen 518055, China

Feng Jin – School of Advanced Materials, Peking University Shenzhen Graduate School, Shenzhen 518055, China

Cong Lin – Department of Applied Biology and Chemical Technology, The Hong Kong Polytechnic University, Hong Kong S.A.R. 999077, China; orcid.org/0000-0003-0021-5055

Zhihao Shen – School of Advanced Materials, Peking University Shenzhen Graduate School, Shenzhen 518055, China

Shiming Chen – Department of Chemistry, The University of Hong Kong, Hong Kong 999077, China

Chunyu Xu – School of Advanced Materials, Peking University Shenzhen Graduate School, Shenzhen 518055, China

Zijin Xu – School of Advanced Materials, Peking University Shenzhen Graduate School, Shenzhen 518055, China

Zhefeng Chen – School of Advanced Materials, Peking University Shenzhen Graduate School, Shenzhen 518055, China

Dong Zhou – School of Advanced Energy, Sun Yat-Sen University Shenzhen Campus, Shenzhen 518107, China; orcid.org/0000-0003-1786-7463

Jun Wang – School of Innovation and Entrepreneurship, Southern University of Science and Technology, Shenzhen 518055, China; orcid.org/0000-0001-9561-5857

Complete contact information is available at:

<https://pubs.acs.org/doi/10.1021/jacs.5c20351>

Author Contributions

[○]W. Zhao and Z. Li contributed equally to this work. The manuscript was written through the contributions of all authors. All authors have given their approval to the final version of the manuscript.

Notes

The authors declare no competing financial interest.

■ ACKNOWLEDGMENTS

This work was financially supported by funding from the National Natural Science Foundation of China (Grant No. 92472206), the Major Science and Technology Infrastructure

Project of Material Genome Big-science Facilities Platform supported by the Municipal Development and Reform Commission of Shenzhen, the International Joint Research Center for Power Battery and Materials (No. 2015B01015), the Guangdong Key Laboratory of Design and Calculation of New Energy Materials (No. 2017B030301013), and the Shenzhen Key Laboratory of New Energy Resources Genome Preparation and Testing (No. ZDSYS201707281026184).

REFERENCES

- (1) Lyu, Y.; Wu, X.; Wang, K.; Feng, Z.; Cheng, T.; Liu, Y.; Wang, M.; Chen, R.; Xu, L.; Zhou, J.; Lu, Y.; Guo, B. An Overview on the Advances of LiCoO₂ Cathodes for Lithium-Ion Batteries. *Adv. Energy Mater.* **2021**, *11* (2), 2000982.
- (2) Xiang, J.; Wei, Y.; Zhong, Y.; Yang, Y.; Cheng, H.; Yuan, L.; Xu, H.; Huang, Y. Building Practical High-Voltage Cathode Materials for Lithium-Ion Batteries. *Adv. Mater.* **2022**, *34* (52), 2200912.
- (3) Fang, J.-J.; Du, Y.-H.; Li, Z.-J.; Fan, W.-G.; Ren, H.-Y.; Yi, H.-C.; Zhao, Q.-H.; Pan, F. J. Surface Structures and Properties of High-Voltage LiCoO₂: Reviews and Prospects. *J. Electrochem.* **2024**, *30* (6), 1.
- (4) Li, Z.; Yi, H.; Ding, W.; Ren, H.; Du, Y.; Shang, M.; Zhao, W.; Chen, H.; Zhou, L.; Lin, H.; Zhao, Q.; Pan, F. Revealing the Accelerated Capacity Decay of a High-Voltage LiCoO₂ upon Harsh Charging Procedure. *Adv. Funct. Mater.* **2024**, *34* (14), 2312837.
- (5) Zhuang, Z.; Wang, J.; Jia, K.; Ji, G.; Ma, J.; Han, Z.; Piao, Z.; Gao, R.; Ji, H.; Zhong, X.; Zhou, G.; Cheng, H.-M. Ultrahigh-Voltage LiCoO₂ at 4.7 V by Interface Stabilization and Band Structure Modification. *Adv. Mater.* **2023**, *35* (22), 2212059.
- (6) Wu, Z.; Zeng, G.; Yin, J.; Chiang, C.-L.; Zhang, Q.; Zhang, B.; Chen, J.; Yan, Y.; Tang, Y.; Zhang, H.; Zhou, S.; Wang, Q.; Kuai, X.; Lin, Y.-G.; Gu, L.; Qiao, Y.; Sun, S.-G. Unveiling the Evolution of LiCoO₂ beyond 4.6 V. *ACS Energy Lett.* **2023**, *8* (11), 4806–4817.
- (7) Hirooka, M.; Sekiya, T.; Omomo, Y.; Yamada, M.; Katayama, H.; Okumura, T.; Yamada, Y.; Ariyoshi, K. Degradation mechanism of LiCoO₂ under float charge conditions and high temperatures. *Electrochim. Acta* **2019**, *320*, 134596.
- (8) Konar, R.; Maiti, S.; Shpigel, N.; Aurbach, D. Reviewing failure mechanisms and modification strategies in stabilizing high-voltage LiCoO₂ cathodes beyond 4.55 V. *Energy Storage Mater.* **2023**, *63*, 103001.
- (9) Weng, C.; Qiu, M.; Wang, B.; Yang, J.; Mai, W.; Pan, L.; Huang, S.; Li, J. Organic Cathode Electrolyte Interphase Achieving 4.8 V LiCoO₂. *Angew. Chem., Int. Ed.* **2025**, *64* (7), No. e202419539.
- (10) Yang, C.; Liao, X.; Zhou, X.; Sun, C.; Qu, R.; Han, J.; Zhao, Y.; Wang, L.; You, Y.; Lu, J. Phosphate-Rich Interface for a Highly Stable and Safe 4.6 V LiCoO₂ Cathode. *Adv. Mater.* **2023**, *35* (14), 2210966.
- (11) Sun, C.; Liao, X.; Xia, F.; Zhao, Y.; Zhang, L.; Mu, S.; Shi, S.; Li, Y.; Peng, H.; Van Tendeloo, G.; Zhao, K.; Wu, J. High-Voltage Cycling Induced Thermal Vulnerability in LiCoO₂ Cathode: Cation Loss and Oxygen Release Driven by Oxygen Vacancy Migration. *ACS Nano* **2020**, *14* (5), 6181–6190.
- (12) Lin, F.; Markus, I. M.; Nordlund, D.; Weng, T.-C.; Asta, M. D.; Xin, H. L.; Doeff, M. M. Surface reconstruction and chemical evolution of stoichiometric layered cathode materials for lithium-ion batteries. *Nat. Commun.* **2014**, *5* (1), 3529.
- (13) Li, Z.; Zhao, W.; Ren, H.; Yi, H.; Du, Y.; Yu, H.; Fang, J.; Song, Y.; Chen, H.; Zhou, L.; Li, S.; Zhao, Q.; Pan, F. Tuning Surface Reconfiguration for Durable Cathode/Electrolyte Interphase of LiCoO₂ at 45 °C. *Adv. Energy Mater.* **2024**, *14* (46), 2402223.
- (14) Huang, W.; Li, J.; Zhao, Q.; Li, S.; Ge, M.; Fang, J.; Chen, Z.; Yu, L.; Huang, X.; Zhao, W.; Huang, X.; Ren, G.; Zhang, N.; He, L.; Wen, J.; Yang, W.; Zhang, M.; Liu, T.; Amine, K.; Pan, F. Mechanochemically Robust LiCoO₂ with Ultrahigh Capacity and Prolonged Cyclability. *Adv. Mater.* **2024**, *36* (32), 2405519.
- (15) Lin, C.; Li, J.; Yin, Z.-W.; Huang, W.; Zhao, Q.; Weng, Q.; Liu, Q.; Sun, J.; Chen, G.; Pan, F. Structural Understanding for High-Voltage Stabilization of Lithium Cobalt Oxide. *Adv. Mater.* **2024**, *36* (6), 2307404.
- (16) Bi, Z.; Yi, Z.; Zhang, L.; Wang, G.; Zhang, A.; Liao, S.; Zhao, Q.; Peng, Z.; Song, L.; Wang, Y.; Zhao, Z.; Wei, S.; Zhao, W.; Shi, X.; Li, M.; Ta, N.; Mi, J.; Li, S.; Das, P.; Cui, Y.; Chen, C.; Pan, F.; Wu, Z.-S. Ultrathin dense LiF coverage coupled with a near-surface gradient fluorination lattice enables fast-charging long-life 4.6 V LiCoO₂. *Energy Environ. Sci.* **2024**, *17* (8), 2765–2775.
- (17) Hu, E.; Li, Q.; Wang, X.; Meng, F.; Liu, J.; Zhang, J.-N.; Page, K.; Xu, W.; Gu, L.; Xiao, R.; Li, H.; Huang, X.; Chen, L.; Yang, W.; Yu, X.; Yang, X.-Q. Oxygen-redox reactions in LiCoO₂ cathode without O-O bonding during charge-discharge. *Joule* **2021**, *5* (3), 720–736.
- (18) Chen, Z.; Lu, Z.; Dahn, J. R. Staging Phase Transitions in Li_xCoO₂. *J. Electrochem. Soc.* **2002**, *149* (12), A1604.
- (19) Li, S.; Sun, Y.; Gao, A.; Zhang, Q.; Lu, X.; Lu, X. Sustainable LiCoO₂ by collective glide of CoO₆ slabs upon charge/discharge. *Proc. Natl. Acad. Sci. U. S. A.* **2022**, *119* (20), No. e2120060119.
- (20) Yan, Y.; Chen, D.; Sun, Z.; Zheng, Q.; Li, W.; Xue, J.; Chen, Y.; Wang, C.; Wang, C.-W.; Liao, H.-G.; Zhang, P.; Qu, C.; Wang, J.-W.; Sun, Y.; Zhang, Q.; Qiao, Y.; Sun, S.-G. Converting and Fabricating LiCoO₂ Cathode Material into a Disordered Rocksalt Surface Modification Layer to Enhance Interfacial Stability of High-Voltage Cathode. *Angew. Chem., Int. Ed.* **2025**, *137* (39), No. e202512300.
- (21) Ding, W.; Ren, H.; Li, Z.; Shang, M.; Song, Y.; Zhao, W.; Chang, L.; Pang, T.; Xu, S.; Yi, H.; Zhou, L.; Lin, H.; Zhao, Q.; Pan, F. Tuning Surface Rock-Salt Layer as Effective O Capture for Enhanced Structure Durability of LiCoO₂ at 4.65 V. *Adv. Energy Mater.* **2024**, *14* (13), 2303926.
- (22) Zhao, W.; Li, M.; Li, Z.; Ren, H.; Wang, X.; Yin, X.; Ding, W.; Chen, G.; Chen, S.; Yi, H.; Li, S.; Wang, J.; Zhou, D.; Zhou, L.; Lin, H.; Fei, B.; Pan, F.; Zhao, Q. Stabilizing Surface Lattice Oⁿ⁻ (0 < n < 2) for Long-Term Durability of LiCoO₂. *Angew. Chem., Int. Ed.* **2025**, *64* (23), No. e202503100.
- (23) Shi, B.; Hu, S.; Feng, J.; Zhou, Y.; Liu, J.; Zhang, J.; Li, W. Titanium and fluorine co-modification strengthens high-voltage electrochemical performance of LiCoO₂. *J. Alloys Compd.* **2022**, *909*, 164787.
- (24) Tan, X.; Zhang, Y.; Xu, S.; Yang, P.; Liu, T.; Mao, D.; Qiu, J.; Chen, Z.; Lu, Z.; Pan, F.; Chu, W. High-Entropy Surface Complex Stabilized LiCoO₂ Cathode. *Adv. Energy Mater.* **2023**, *13* (24), 2300147.
- (25) Xu, S.; Tan, X.; Ding, W.; Ren, W.; Zhao, Q.; Huang, W.; Liu, J.; Qi, R.; Zhang, Y.; Yang, J.; Zuo, C.; Ji, H.; Ren, H.; Cao, B.; Xue, H.; Gao, Z.; Yi, H.; Zhao, W.; Xiao, Y.; Zhao, Q.; Zhang, M.; Pan, F. Promoting Surface Electric Conductivity for High-Rate LiCoO₂. *Angew. Chem., Int. Ed.* **2023**, *135* (10), No. e202218595.
- (26) Bawane, K.; Manganaris, P.; Wang, Y.; Sure, J.; Ronne, A.; Halstenberg, P.; Dai, S.; Gill, S. K.; Sasaki, K.; Chen-Wiegart, Y.-c. K.; Gakhar, R.; Mahurin, S.; Pimblott, S. M.; Wishart, J. F.; He, L. Determining oxidation states of transition metals in molten salt corrosion using electron energy loss spectroscopy. *Scr. Mater.* **2021**, *197*, 113790.
- (27) Li, S.; Li, K.; Zheng, J.; Zhang, Q.; Wei, B.; Lu, X. Structural Distortion-Induced Charge Gradient Distribution of Co Ions in Delithiated LiCoO₂ Cathode. *J. Phys. Chem. Lett.* **2019**, *10* (24), 7537–7546.
- (28) Wang, Z.; Lee, J. Z.; Xin, H. L.; Han, L.; Grillon, N.; Guy-Bouyssou, D.; Bouyssou, E.; Proust, M.; Meng, Y. S. Effects of cathode electrolyte interfacial (CEI) layer on long term cycling of all-solid-state thin-film batteries. *J. Power Sources* **2016**, *324*, 342–348.
- (29) Saitoh, M.; Gao, X.; Ogawa, T.; Ikuhara, Y. H.; Kobayashi, S.; Fisher, C. A. J.; Kuwabara, A.; Ikuhara, Y. Systematic analysis of electron energy-loss near-edge structures in Li-ion battery materials. *Phys. Chem. Chem. Phys.* **2018**, *20* (38), 25052–25061.
- (30) Qin, N.; Gan, Q.; Zhuang, Z.; Wang, Y.; Li, Y.; Li, Z.; Hussain, I.; Zeng, C.; Liu, G.; Bai, Y.; Zhang, K.; Lu, Z. Hierarchical Doping Engineering with Active/Inert Dual Elements Stabilizes LiCoO₂ to 4.6 V. *Adv. Energy Mater.* **2022**, *12* (31), 2201549.

(31) Zhang, K.; Yang, T.; Chen, T.; Yang, Y.; Jiang, Z.; Gao, C.; Zuo, Y.; Xiao, W.; Xia, D. An amorphous Li–V–O–F cathode with tetrahedral coordination and O–O formal redox at low voltage. *Nat. Mater.* **2025**, *24* (10), 1600–1607.

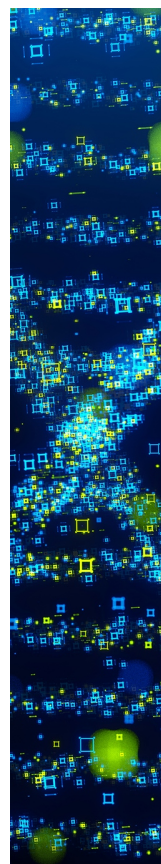
(32) Qin, R.; Ding, S.; Hou, C.; Liu, L.; Wang, Y.; Zhao, W.; Yao, L.; Shao, Y.; Zou, R.; Zhao, Q.; Li, S.; Pan, F. Modulating the Proton-Conducting Lanes in Spinel ZnMn_2O_4 through Off-Stoichiometry. *Adv. Energy Mater.* **2023**, *13* (20), 2203915.

(33) Wang, C.; Jing, Y.; Zhu, D.; Xin, H. L. Atomic Origin of Chemomechanical Failure of Layered Cathodes in All-Solid-State Batteries. *J. Am. Chem. Soc.* **2024**, *146* (26), 17712–17718.

(34) Zhu, D.; Wang, C.; Zou, P.; Zhang, R.; Wang, S.; Song, B.; Yang, X.; Low, K.-B.; Xin, H. L. Deep-Learning Aided Atomic-Scale Phase Segmentation toward Diagnosing Complex Oxide Cathodes for Lithium-Ion Batteries. *Nano Lett.* **2023**, *23* (17), 8272–8279.

(35) Wang, C.; Wang, X.; Zou, P.; Zhang, R.; Wang, S.; Song, B.; Low, K.-B.; Xin, H. L. Direct observation of chemomechanical stress-induced phase transformation in high-Ni layered cathodes for lithium-ion batteries. *Matter* **2023**, *6* (4), 1265–1277.

(36) Yan, Y.; Fang, Q.; Kuai, X.; Zhou, S.; Chen, J.; Zhang, H.; Wu, X.; Zeng, G.; Wu, Z.; Zhang, B.; Tang, Y.; Zheng, Q.; Liao, H.-G.; Dong, K.; Manke, I.; Wang, X.; Qiao, Y.; Sun, S.-G. One-Step Surface-to-Bulk Modification of High-Voltage and Long-Life LiCoO_2 Cathode with Concentration Gradient Architecture. *Adv. Mater.* **2024**, *36* (1), 2308656.



CAS BIOFINDER DISCOVERY PLATFORM™

STOP DIGGING THROUGH DATA —START MAKING DISCOVERIES

CAS BioFinder helps you find the
right biological insights in seconds

Start your search

